



Delft University of Technology

Battery-less uncertainty-based control of a stand-alone PV-electrolyzer system

Martinez Lopez, V. A.; Isabella, O.; Zeman, M.; Ziar, H.

DOI

[10.1016/j.jpowsour.2024.234934](https://doi.org/10.1016/j.jpowsour.2024.234934)

Publication date

2024

Document Version

Final published version

Published in

Journal of Power Sources

Citation (APA)

Martinez Lopez, V. A., Isabella, O., Zeman, M., & Ziar, H. (2024). Battery-less uncertainty-based control of a stand-alone PV-electrolyzer system. *Journal of Power Sources*, 614, Article 234934. <https://doi.org/10.1016/j.jpowsour.2024.234934>

Important note

To cite this publication, please use the final published version (if applicable). Please check the document version above.

Copyright

Other than for strictly personal use, it is not permitted to download, forward or distribute the text or part of it, without the consent of the author(s) and/or copyright holder(s), unless the work is under an open content license such as Creative Commons.

Takedown policy

Please contact us and provide details if you believe this document breaches copyrights. We will remove access to the work immediately and investigate your claim.



Battery-less uncertainty-based control of a stand-alone PV-electrolyzer system

V.A. Martinez Lopez^{*}, O. Isabella, M. Zeman, H. Ziar

Photovoltaic Materials and Devices group of Delft University of Technology, Delft, 2628CD, The Netherlands

HIGHLIGHTS

- Application of forecasting for power smoothing.
- Uncertainty-based prediction.
- Control decision considering the uncertainty.
- Power ramp smoothing without electric storage.

ARTICLE INFO

Keywords:

Nowcasting
Active power curtailment
PV-hydrogen systems
Uncertainty
Fuzzy logic

ABSTRACT

Solar photovoltaic (PV) energy is variable. The output power can change considerably in a matter of minutes, imposing challenges on the control of systems connected downstream. The power from these systems can be smoothed using electric storage, potentially increasing the system cost. An alternative is to deliberately curtail the power before it starts to change. This strategy relies on ultra-short-term forecasting to determine the curtailment point. Unfortunately, forecasting is prone to errors and high uncertainty even in the very short-term, leading to control errors. We propose an active power curtailment control strategy for a stand-alone solar photovoltaic system powering an electrolyzer. Our work's novelty relies on the controller's ability to deal with large forecasting errors and high uncertainty, combining artificial intelligence for predicting the power ramps and fuzzy logic to account for imperfect prediction. We validated our approach using a hardware emulator of the photovoltaic system, power converter and electrolyzer. Under clear sky conditions, the curtailment results in unnecessary energy loss, while under variable irradiance, the controller successfully smooths the power ramps within 10% of the PV system's nominal power. Although our approach was designed for a stand-alone system, its concept can be directly applied to grid-connected systems as well.

1. Introduction

Renewable energy has grown significantly in the last years and is expected to cover as much as 38% of the world's electricity mix by 2027 [1]. In particular, solar energy is the most rapidly expanding technology, exceeding the expectations by a 30% [1]. Solar energy is highly variable and, due to passing clouds, it can result in sudden and significant power changes of a PV plant. These changes, often called *ramps* can have consequences on the network to which the plant is connected. For grid-connected systems, these changes might negatively influence the grid voltage and frequency [2]. Furthermore, grid operators often impose limits on the allowed changes of power. For example, Germany and Puerto Rico establish a ramp rate limit of 10%/min [3]. A straightforward solution to power ramps of PV systems is to add electric storage, but this is not a fixed requirement

to do power smoothing. This objective can also be fulfilled by curtailing the output PV power during a ramp event. For ramp-up events, this is straightforward, as the power can be curtailed to the current production level and slowly climb to the new maximum power point, thus avoiding a ramp violation. On the other hand, for a ramp-down event, the power will drop immediately if no storage is available. To prevent this, the power must be slowly curtailed *before* the event [4]. Battery-less smoothing techniques also result in lower leveled costs of electricity, especially when the smoothing requirement is small because the investment costs of batteries exceed the cost of loss of energy due to curtailment. However, this is only true when the prediction of ramps is highly accurate [5]. In the stand-alone case, PV-electrolyzer systems for hydrogen production can be operated with or without batteries. The advantage of battery-assisted electrolysis is a constant operation despite

^{*} Corresponding author.

E-mail address: V.A.MartinezLopez@tudelft.nl (V.A. Martinez Lopez).

the variations in irradiance, and the production during nighttime [6]. Also, in these systems, curtailment might be the cheapest option for off-grid operation of solar-hydrogen systems [7].

Since battery-less power smoothing relies on short-term forecasting (nowcasting), this tool becomes an essential ramp control [4,8–10]. As an example, an algorithm of a power management system relies on nowcasting as a first step to perform power smoothing based on signal processing techniques [10]. For PV systems, a method using a sky image facilitates determining whether or not a cloud will (partially) block the sun. This information allows the estimation of the drop in PV power, which determines the active power curtailment needed to smooth the ramp [11]. Also, in this approach, the performance of the smoothing approach depends heavily on the quality of the prediction.

These systems require a high level of prediction accuracy to perform the control [4,10] which is not achieved in practice. Nowcasting irradiance ramps is a challenging task and even systems with artificial intelligence fail to predict irradiance events in the very short term. While some authors have discussed that knowledge on the accuracy of predictions can improve the control strategies [8], how to include such knowledge is not mentioned. Some strategies to deal with the forecasting inaccuracy include using reinforced learning to adapt the power curtailment even with low-quality predictions [12]. This study tackles the problem of the inherent inaccuracy of ultra-short-term forecasting (nowcasting) when applied to a smoothing technique based on active power curtailment. Its novelty relies on combining the knowledge of the forecasting uncertainty with fuzzy logic to smooth the power from an off-grid PV system feeding an alkaline electrolyzer. An experimental setup validates the control strategy emulating the off-grid PV-electrolyzer system. Section 2 describes the models used (Sections 2.1.1 and 2.1.2), while the experimental setup is introduced in Section 2.2. The prediction module is presented in (Section 2.3.1) along with the fuzzy logic controller (Section 2.3.2). Section 3 reports the results and the discussion before the conclusion, presented in Section 4.

2. Methodology

This work proposes a battery-less, uncertainty-based power smoothing technique for a stand-alone PV-electrolyzer system. We validated the operation of our technique with a hardware setup that emulates the system. The emulation of this system requires three domains: a physical domain that emulates the PV system, the electronic converter that controls the PV system, and the electrolyzer, a modeling domain that describes the behavior of the physical domain so it closely represents a real system, and a control domain which supervises and controls the whole system. Fig. 1 provides an overview of the system, and the corresponding domains. Each of these domains is explained in detail below.

2.1. Modeling domain

2.1.1. PV model

The emulated PV system consists of 6 PV modules connected in series, with a total peak power of 2700 W. The PV module used as a reference is a TRINA TALLMAX-M 450 [13]. The modules share the same tilt ($a_m = 19^\circ$) and azimuth ($A_s = 185^\circ$). The size and orientation of this system come from an optimization procedure for stand-alone PV hydrogen systems as described in [14]. The model of this system is a set of current–voltage (I–V) curves, one per simulation step, calculated from measured irradiance and ambient temperature. The monitoring station of the Photovoltaic Materials and Devices (PVMD) group of TU Delft (latitude 51.9997° , longitude 4.3689°) recorded the 1-min Global Horizontal Irradiance (GHI) using a silicon pyranometer on 13-June-2021 (clear day) and 31-July-2021 (variable day).

The calculation of the module's I–V curve at a specific irradiance level requires the knowledge not of the horizontal irradiance, but

the irradiance impinging on the PV module (Plane-Of-Array, POA, irradiance), and for this, the direct and diffuse components are needed.

The DISC decomposition model [15] allows the retrieval of the Direct Normal Irradiance (DNI) from the Global Horizontal Irradiance (GHI). The implementation of this model is readily available as a MATLAB function from PV LIB [16]. Eq. (1) shows the calculation of the Diffuse Horizontal Irradiance (DHI) from the GHI and the sun's elevation angle, a_s [17].

$$DHI = GHI - DNI \cdot \sin(a_s) \quad (1)$$

These three quantities allow the calculation of the Plane-of-array irradiance G_{POA} . Eq. (2) [17] shows the calculation of G_{POA} . Note that it includes the three irradiance components obtained before. The Greek letters ρ and γ correspond to the albedo (assumed constant, with a value of 0.2) and the angle between the sun and the PV module, (calculated by MATLAB PVLIB's function `pv_getaoi`), respectively.

$$G_{POA} = DNI \cdot \cos \gamma + DHI \cdot SVF + \rho \cdot GHI \cdot (1 - SVF) \quad (2)$$

The model assumes an isotropic sky. This assumption implies that the diffuse irradiance is the same across the sky dome and the portion of the sky that the module, tilted at an angle a_m , sees (sky view factor) is simplified as in Eq. (3) [17].

$$SVF = \frac{1 + \cos a_m}{2} \quad (3)$$

Following the procedure in [18], the plane-or-array irradiance, combined with a two-diode model leads to the calculation of the module's I–V curve at each irradiance point.

2.1.2. Electrolyzer model

The electrolyzer is simulated as a power–voltage curve of a fictitious 1280 W, alkaline electrolyzer. This power is 2.1 times smaller than the nominal power of the PV system, following the optimization procedure described in [14].

A current–voltage curve models the electrolyzer. When the current flows through the electrolyzer, its voltage increases as the electrons must overcome energy barriers for the chemical reaction that decomposes water into hydrogen and oxygen molecules. These barriers are the reversible voltage (minimum energy that the reaction needs, considered as 1.229 V) and overvoltages. We consider only the activation overvoltage (energy of the reaction at the electrodes) described by a modified version of the Tafel equation. Eq. (4) gives the current–voltage characteristic of the electrolyzer [19].

$$I = I_0 \exp\left(\left(\frac{F}{RT}\right)\left(\frac{V}{n_{\text{cells}}} + 1.229\right)\right) \quad (4)$$

Its parameters are the universal gas constant ($R = 8.314 \frac{\text{J}}{\text{molK}}$), Faraday's constant ($F = 9.64 \times 10^4 \text{ C}$), Temperature ($T = 333.15 \text{ K}$), exchange current ($I_0 = 1.8 \times 10^{-7} \text{ A}$), and the number of cells in the stack ($n_{\text{cells}} = 244$). This last one was adjusted so the electrolyzer voltage would lay between 300 and 400 V to avoid problems with the protections of the inverter (see Section 2.2 for an explanation of the setup). The power of the electrolyzer is the product of its current and voltage. Ten voltage levels were defined, ranging from 300 to 400 V, and at each point, the power was computed using Eq. (4) multiplied by the corresponding voltage. The voltage of the electrolyzer, as a function of the input power, is derived from these points and implemented in a lookup table. Except for the physical constants, the parameters used in Eq. (4) are fictitious.

The production of hydrogen (h_2 , mol/s) is proportional to the current, I , flowing through every cell of the electrolyzer (number of cells, n_{cells}) according to Faraday's law of electrolysis (Eq. (5)).

$$h_2 = \eta_F \frac{I}{2F} n_{\text{cells}} \quad (5)$$

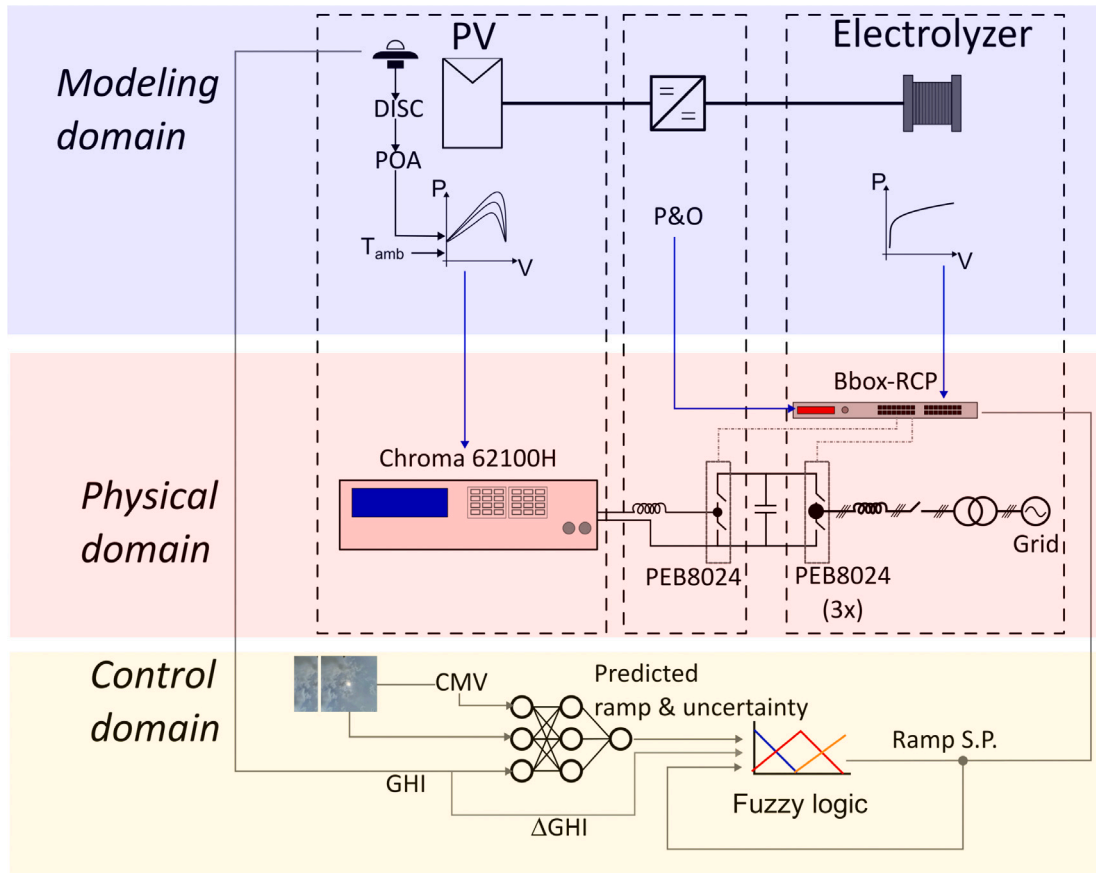


Fig. 1. Overview of the implemented system. The physical domain consists of a DC power supply (Chroma 62100H), a boost converter, and a three-phase grid-tied inverter built from Imperix PEB8024 half-bridge modules. An FPGA board (Imperix Bbox RCP) controls the switches of the boost converter and of the three-phase inverter. On top of the physical domain, a modeling domain describes how the hardware reproduces the real system signals. The PV model consists of a set of current–voltage curves calculated from measured data using the DISC decomposition model, a transposition model to calculate the Plane-of-Array irradiance, and a two-diode model. The boost converter controlling the PV system performs a modified Perturb-and-Observe (P&O) Maximum Power Point Tracking (MPPT) algorithm. The inverter uses the Power–Voltage curve of the electrolyzer to set its input voltage according to the received power, following the electric behavior of the electrolyzer. The control domain sets the reference points that ultimately perform the power smoothing. It relies on an artificial intelligence module making one-minute ahead predictions of the ramps and the uncertainty associated with such prediction. Its output feeds a fuzzy logic model that outputs the ramp set point, which is sent back to the Bbox-RCP in the physical domain. CMV, GHI and S.P. stand for *Cloud Motion Vector*, *Global Horizontal Irradiance* and *set point*, respectively.

The Faraday efficiency, η_F , describes losses caused by the current not flowing through the electrodes (parasitic currents). This phenomenon increases at low current density, i , as described by Eq. (6) [20].

$$\eta_F = \frac{i^2}{f_1 + i^2} f_2 \quad (6)$$

where the fitting parameters are $f_1 = 2 \times 10^4 \text{ A}^2/\text{m}^4$ and $f_2 = 0.985$ (dimensionless) [20].

2.2. Physical domain (Experimental setup)

The experimental setup consists of two main parts. A solar I–V curve emulator and a power electronics module which concurrently performs the MPPT and emulates the electrolyzer’s P–V curve. The solar emulator is a Chroma 62100H - 600S DC-power source. Its software allows the reproduction of a PV system I–V curve which can be programmed to change in time [21]. The interface between the electrolyzer and the PV system (output of DC power supply) is a boost converter, responsible for controlling the PV system’s output either by performing maximum power point tracking (MPPT) or setting a specific power set point. This converter is connected to a three-phase inverter. Both converters are implemented using Imperix PEB8024 (half-bridge) power modules and power filters [22,23]. The Imperix Bbox-RCP unit controls the power

modules [24]. The control of all the converters can be easily developed using MATLAB Simulink and sent to the Bbox-RCP.

The Perturb & Observe (P&O) maximum power point tracking algorithm extracts the maximum power from the PV system. The modification proposed in [25] allows a deliberate operation of the PV system at a different power point rather than the maximum (i.e. curtailment) with only a small change in the original P&O algorithm. This algorithm drives a boost converter (interface between the PV system and electrolyzer) and is implemented in the Bbox-RCP unit. Varying the voltage of the DC-link between the boost converter and the inverter according to the P–V curve of the electrolyzer allows the emulation of this component. The P–V curve of the electrolyzer is also implemented as a lookup table in the Bbox-RCP unit. Note that although the inverter is connected to the grid, the system is not a grid-connected system. This connection is there to dissipate the generated power, that in a real system will be consumed by the electrolyzer. **The emulated system is a stand-alone (off-grid) system.**

2.3. Control domain

2.3.1. Irradiance prediction module

The irradiance prediction module predicts one-minute-ahead ramps of the global horizontal irradiance (GHI). In this work, a ramp is defined as the percentage of change with respect to the last measured GHI value. Rather than a single value, the model outputs the probability

that a certain set of inputs belongs to a ramp class. By doing this, it is possible to retrieve information not only on the most probable ramp that will occur but also a measure of uncertainty of the prediction.

The model is based on neural networks whose input are, a single low-resolution (64×64 pixels) sky image centered around the sun, last measured GHI, and cloud motion vector. The sky images were taken using an all-sky imager (CMS-Shreder ASI-16 [26]) equipped with a fisheye lens located at the above-mentioned PVMD group monitoring station. The sky images are taken every minute, along with the global horizontal irradiance (GHI), measured with a silicon pyranometer provided with the sky imager. The high-resolution images are first corrected to remove the fish eye distortion, cropped around the sun (200×200 pixels), and then resized to a resolution of 64×64 pixels. Using optical flow from two consecutive images it is possible to calculate the cloud motion vector which returns the direction and speed of the main cloud layer and is expressed in cartesian coordinates whose origin is the center of the sky image, which is also the center of the sun.

The Farneback optical flow [27] is an image-processing method that determines the vectors indicating how the pixels of two consecutive images are moving. This pre-processing step returns all the vectors of the pixels moving between two sky images. Since most of the pixels remain static, a histogram of the directions of the vectors will exhibit a bimodal distribution with one mode close to zero and the second indicating the main cloud direction. The mean magnitude of the vectors in this direction is the main cloud speed [28]. In practice, the cloud motion vector is obtained by running a clustering algorithm (k-means) with two clusters of magnitudes and directions obtained from the optical flow. All values smaller than one standard deviation of each vector component are excluded from the clustering (still pixels). The largest of the two cluster centroids obtained through k-means is the cloud motion vector (in pixels per minute) [28].

The neural network comprises two stages: one responsible for the processing of the sky image, and the second which combines the image analysis output with the auxiliary data (GHI, X and Y components of the cloud motion vector). Fig. 2 shows the architecture of the neural networks. The network responsible for processing the sky image is a ResNet50 implemented in the Keras library [29]. The auxiliary data network is a fully connected network of 3 layers with 64, 32, and 1 neurons, respectively. The first two layers use the Rectified Linear Unit (ReLU) activation function, and the output layer uses a softmax activation function. The training loss is the sparse categorical loss entropy. Note that this is a *classification* problem rather than a *regression* one. As such, the softmax function of the last layer returns the probability that a particular set of inputs belongs to one of the labeled classes. The labeled classes are 20 ramp bins with equal *frequency* in each bin, which means that the width of the bins is different, but the number of elements is approximately the same. The labels are coded as integers from 1 to 20. The class with the highest probability is the predicted class. Since each class label is linked to a bin, the actual predicted ramp is the center of the bin corresponding to that particular class. A cumulative sum of the probabilities of all the classes allows the determination of the 5th and 95th percentiles; their difference is a measure of uncertainty. These two outputs, the predicted ramp (the bin center of the most probable class) and the uncertainty (the difference between the 5th and 95th percentiles of the cumulative sum of the probabilities of all classes), are inputs to the fuzzy logic control. The training set consists of 27,723 samples and the validation set of 7431 samples.

2.3.2. Fuzzy logic controller

Fuzzy logic offers a solution to complex systems by describing them as linguistic variables rather than complicated equations. The relations between the inputs and outputs (already described by linguistic variables) are written using a set of if/then rules. This makes handling the uncertainties and imprecision of the model an easy task. Fuzzy logic as opposed to traditional set theory, relies on the fact that an element can

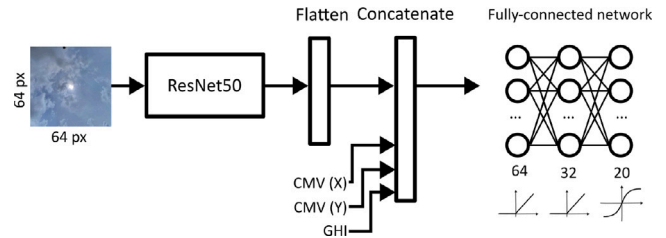


Fig. 2. Architecture of the prediction module. The acronym “CMV” refers to the cloud motion vector; each component of this vector, X and Y, is a separate input to the model. GHI is the Global Horizontal Irradiance. The fully-connected network has two hidden layers with 64 and 32 neurons with a Rectified Linear Unit (ReLU) as activation function. The output layer consists of 20 neurons (one per bin) with the softmax activation function.

Table 1

Fuzzy controller variables and their linguistic descriptors.

Variable name	Linguistic descriptor
Inputs	
Δ GHI	Negative large, shallow, positive high
Predicted ramp	Deep down, shallow, deep up
Previous slope	Negative big, zero, positive big
Uncertainty	Low, high
Output	
Slope	Negative large, zero, positive large

simultaneously (and partially) be a member of more than one set. In other words, its degree of membership to a set is not a binary (yes/no) function, but a continuous one. And this is mapped by a membership function. Membership functions are useful in the *fuzzyfication* step, where a *crisp* variable value is transformed into a *fuzzy* variable. The linguistic variables are also linked to the membership functions in the sense, that a variable “slow” can be described by a particular membership function. The if/then rules describe the relation between the system variables and constitute the implication step of a fuzzy system (e.g. if TEMPERATURE is COLD then SPEED is FAST). These are translated as minimum and maximum operators (equivalent to the intersection and union of the traditional set theory) [30].

Our model used the *Mamdani min* implication rule, which is the minimum value of both input and output membership functions. This rule typically results in clipping the output membership function at the value of the input membership function, evaluated at the crisp input. Converting the fuzzy output back to a crisp number is done by calculating the centroid of the clipped output membership function [30].

The fuzzy control model takes four inputs, every minute: the predicted ramp (from the Prediction Module), the uncertainty of the prediction (from the Prediction module), the last observed change in the Global Horizontal Irradiance (Δ GHI), and the previous slope applied. The output is the slope (given as a percentage of change with respect to the nominal power). This slope defines the power set point sent to the system, every second. Using Δ GHI instead of the Plane-of-array irradiance (G_{POA}) allows a generalization of our approach (Δ GHI is not system dependent as G_{POA}).

Table 1 shows the system variables and their corresponding fuzzy descriptors and Fig. 3(a) shows the membership functions for all the inputs (Figs. 3(a), 3(b), 3(c), and 3(d)) and the output (Fig. 3(e)). A description of the fuzzy rules can be found in Appendix.

3. Results

We used two scenarios to test our control strategy. Fig. 4 shows the GHI of both scenarios along with the portion of the day considered for the experiments. The first scenario corresponds to a clear day (13-June-2021, Fig. 4(a)). The second scenario is a day with high irradiance

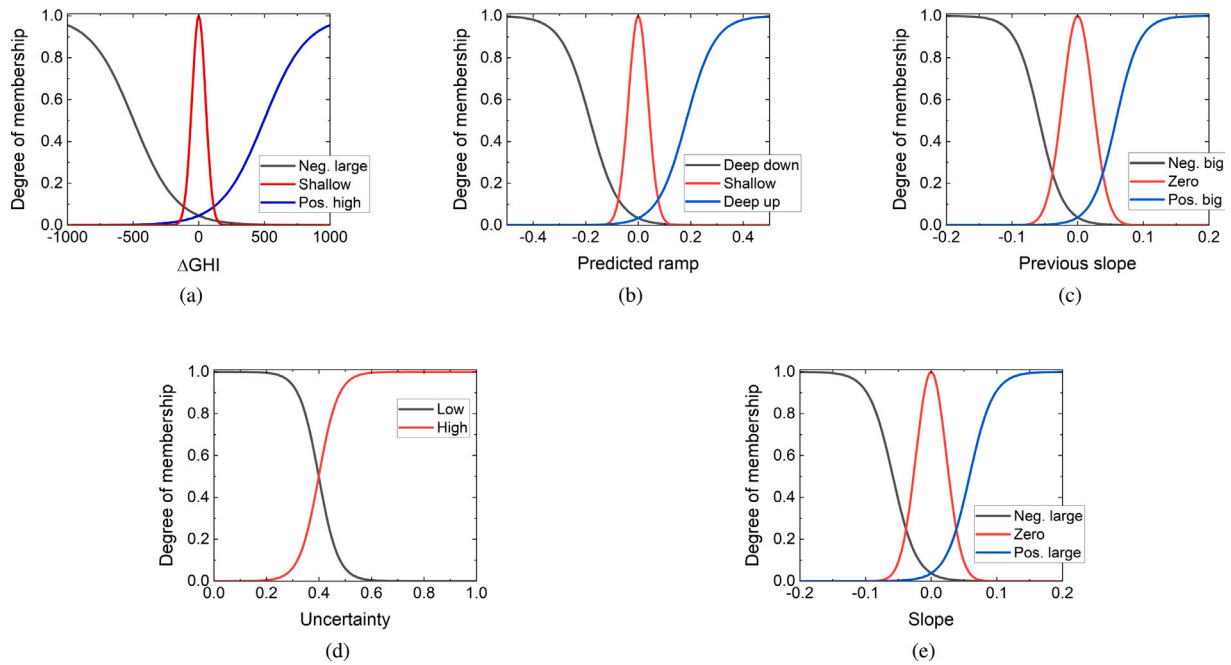


Fig. 3. Membership functions of the fuzzy logic controller of (a) the irradiance changes, ΔGHI , (b) the predicted ramp, (c) the previous slope. (c) The uncertainty. Note that everything above 0.5 is classified as “high” and everything below 0.3 as “low” uncertainty. The region between these numbers is fuzzy can be “high” and “low”. (d) The output slope.

variability (31-July-2021, Fig. 4(b)). The reader must be aware that the results are presented in two time resolutions: the instantaneous, which is 1 s resolution and is the time resolution at which the controller acts. In other words, it sends a power set point every second (see Section 2.3.2). The irradiance and prediction data have a lower time resolution, namely one minute. The downsampling of the 1-s data to 1-min resolution takes place using the median every 60 s. The median is less sensitive to extreme values, present within the variable scenario, and the mode can either be non-existent or have multiple values, especially with a small sample (60 points). Hence we consider that the median can represent better the 1-min value.

3.1. Ramp prediction

The prediction model has a training accuracy of 19.51% and a validation accuracy of 17.29%. Note that the training dataset is relatively small, which can be one of the causes of the low accuracy. Many of the samples also correspond to images with the sun blocked. Identifying the sun automatically is almost straightforward, through identifying the brightest pixels on the image [31]. However, when the sun is covered, its location on the image needs to be estimated based on the sun’s position in the sky. Although the estimation accurately identifies the sun’s position, when the image is cropped around the sun, the estimation error causes the sun not to be centered in the cropped image. The mismatch error on cloudy images is larger because the image is first corrected, and the sun is identified afterward. This can have negative consequences downstream, because the cloud motion vector is estimated from two consecutive *cropped* images, and it assumes that the sun is in the middle of the image.

The calculation of the cloud motion vector might also be responsible for the low prediction accuracy. It is calculated from the optical flow results followed by a k-means clustering algorithm (see Section 2.3.1). The optical flow returns the apparent movement of *pixels* between two consecutive images. The main assumption is that the difference between the two consecutive images, especially taken one minute apart, is the movement of clouds. Although we applied a smoothing filter on the image to remove noise, the movement of pixels might not entirely correspond to clouds. Changes in the tone of the sky, clouds, objects

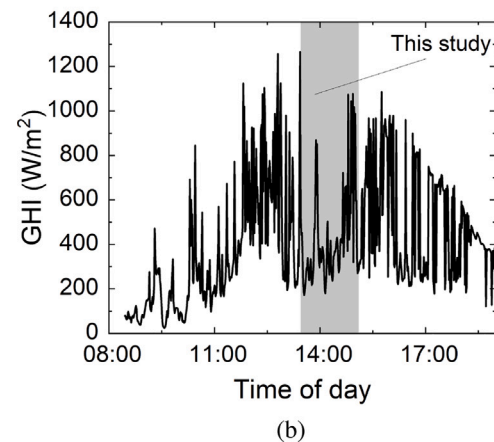
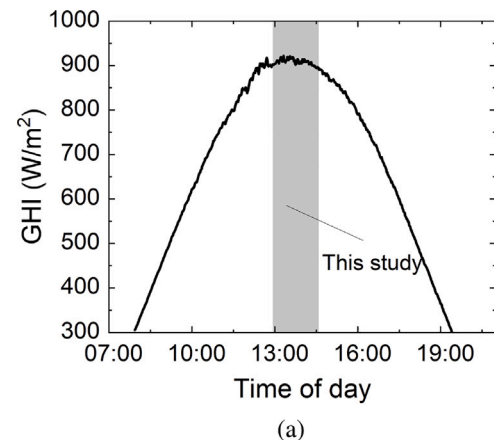
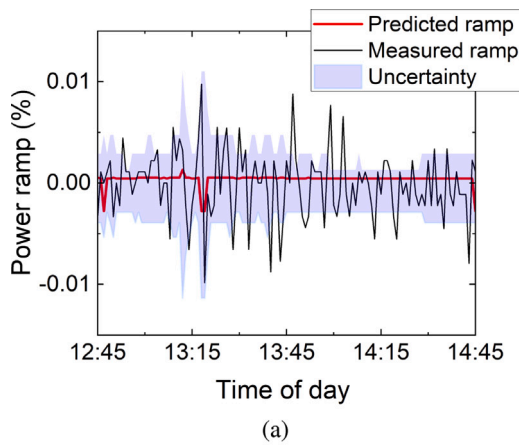
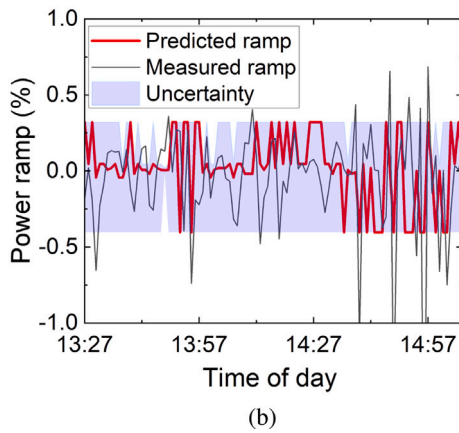


Fig. 4. Global Horizontal Irradiance of the two used scenarios. (a) a clear day, and (b) a variable day. In both graphs, the shaded area marked as “This study” shows the period used for the experiments.



(a)



(b)

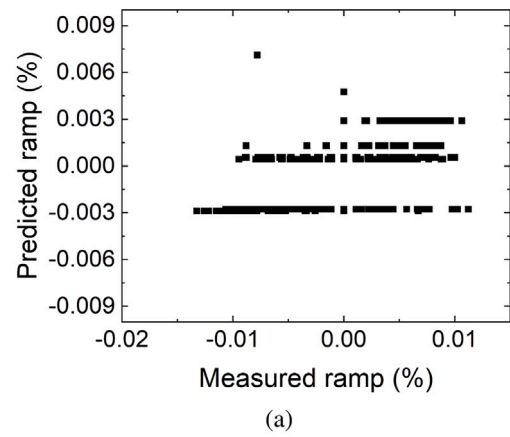
Fig. 5. Example of ramp prediction of (a) the clear scenario and (b) the variable scenario.

moving on the scene, and glare, among others, might be identified as moving pixels and can affect the estimation of the cloud motion vector.

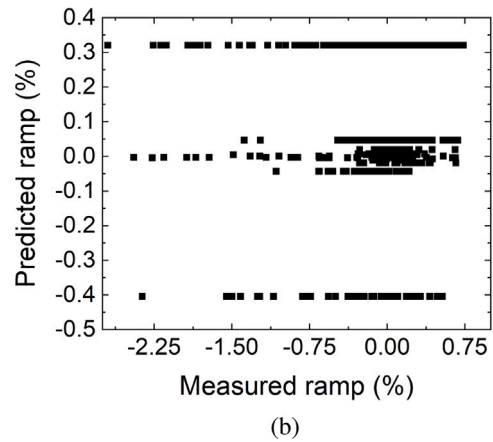
Fig. 5 shows an example of the prediction for the interval used for the clear and variable scenarios shown in Fig. 4. For the clear scenario (Fig. 5(a)), the output is basically a constant that is lower than the measured ramps. Many measured points fall into the uncertainty range, as desired. For the variable case (Fig. 5(b)), the discrepancy between the measured and the predicted ramps and the uncertainty is higher. Note that, in Fig. 5(b), the predicted ramp and uncertainty seem to saturate at $\pm 0.4\%$. This behavior and the constant output of Fig. 5(a) might be attributed to the binning method used for training the data (see Section 2.3.1). Each ramp bin has a different width and assigned a number to identify it. Hence the values that the classifier learns are integers (bin numbers) and not actual ramp values. To retrieve the actual ramp we used the value at the center of each bin as a representative value of the whole bin. The extreme values of this approach are precisely $\pm 0.4\%$.

Fig. 6 shows the measured against the predicted ramps for the clear (Fig. 6(a)) and the variable (Fig. 6(b)) scenarios. Note that the predicted ramps are located only at particular intervals (bin centers) that span over a wide range of measured ramps. Increasing the number of bins can reduce the scattering within each bin and lead to a more accurate prediction.

The prediction result do not need to be accurate because the fuzzy logic will convert these values into a language descriptor (e.g. LOW, LARGE, see Table 1) making it able to deal with the imprecision and uncertainty, which is the main goal of this work.



(a)



(b)

Fig. 6. Measured and predicted ramps of (a) the clear scenario and (b) the variable scenario.

3.2. Ramp control

Fig. 7 shows the results of applying our proposed approach to the clear scenario. Under clear conditions (Fig. 7(a)), our approach always operates in a curtailment condition after the initial system startup. It is worth mentioning, that an initial power drop of 30% was deliberately introduced to avoid problems with the curtailment set point. After this sudden power decrease, the system stabilizes and increases monotonically. For a clear scenario, the ramps are always within the required limits (Fig. 7(b)).

Fig. 8 shows the results for the variable scenario. Similar to the clear scenario, the controller curtails the power most of the time, and under shallow ramps, the controller even keeps the power at a constant level (Fig. 8(a)). This results in an evident ramp smoothing, reducing ramp violations (Fig. 8(b)) and proving that our approach is able to meet the objective.

Fig. 8(a) also shows that the P&O algorithm fails under variable conditions. This occurs because the controller sends a power set point higher than the actual MPP. Note that the P&O implemented in this work is a modified version of the traditional P&O. This version tracks MPP in the absence of a power set point. Otherwise, it uses the same P&O logic to track a curtailment set point [25]. If the power set point is larger than the actual MPP, the algorithm will keep reducing the voltage until it reaches the short-circuit condition, attempting to find a point outside the power-voltage curve of the PV module. The sampling time of the P&O algorithm is 5 ms, which explains the sudden drops in the power of Fig. 8(a). A watchdog timer monitors the PV power to detect and correct this condition. When this timer detects a

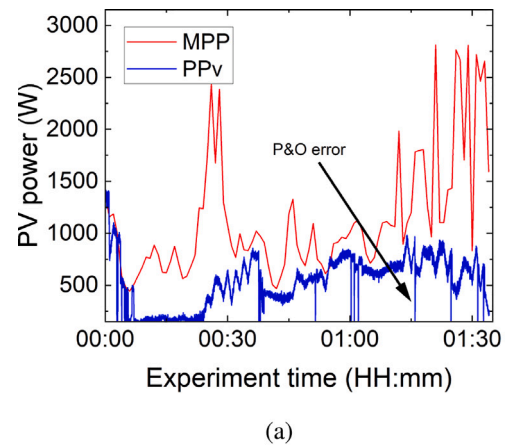
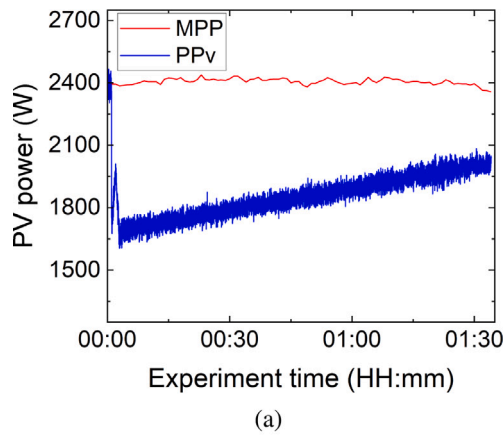


Fig. 7. Results of the clear scenario with 1 s resolution. (a) Instantaneous PV power (PPV), and (b) one-minute PV power ramps, given as a percentage of the nominal PV power, (P_{nom}). The 10% ramp limit is marked as a red band. Points outside these bands are considered ramp violations.

Fig. 8. Results of the variable scenario with 1 s resolution. (a) Instantaneous PV power. Note the sudden power drops to zero as a result of a failure of the P&O algorithm. An example of these peaks is marked with an arrow (“P&O error”). (b) One-minute PV power ramps, given as a percentage of the nominal PV power, (P_{nom}). The 10% ramp limit is marked as a red band. Points outside these bands are considered ramp violations.

faulty condition, it removes the power set point, restoring the normal operation of the algorithm. The failure of the P&O is only visible in the 1 s resolution data. It does not affect the power smoothing results. Note that the aggregation method for the downsampling to 1 min is the median.

Fig. 9 compares the operating point (as a percentage of the maximum power point) of the 1-min resolution data of the clear and variable scenarios. While in the clear moments most of the points are centered around 80% of the theoretical MPP, in the variable scenario, the operating points are more distributed and can even get lower than 20% of the theoretical maximum. This stricter control, needed to smooth 1-min ramps, leads to an energy loss of 53.1% with respect to the theoretical maximum power point. Section 3.3 provides an in-depth discussion on how to improve this aspect.

Applying control to a clear day results in unnecessary power curtailment that can go as low as 70% of the theoretical maximum power point (Fig. 9). The system generates 3.77 kWh during the 100 min at its theoretical maximum power point and 2.91 kWh under controlled power. This represents a loss of 22.8% of the potential generated energy. Because of this, for a clear moment, no control action is needed. An ideal controller should be able to (a) avoid any control action in clear conditions or (b) ensure a minimum curtailment. In this sense, the traditional P&O MPP algorithm is more than suitable. Identifying clear moments before they occur is fundamental to applying the traditional P&O during these moments instead of unnecessarily curtailing energy. Our approach is based on one-minute ahead prediction to smooth

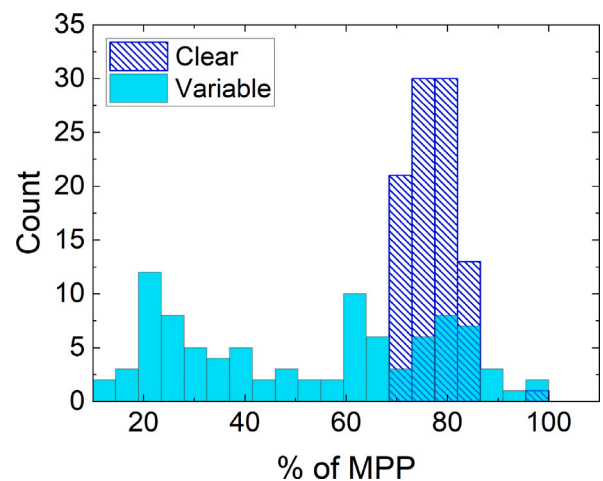


Fig. 9. Distribution of the operating point of both scenarios. The operating point is given as a percentage of the theoretical maximum power point with 1-min resolution.

instantaneous ramps. With a single-prediction value it is impossible to identify clear moments. Using historical data could give an indication of the present conditions. The probability that the sky conditions remain

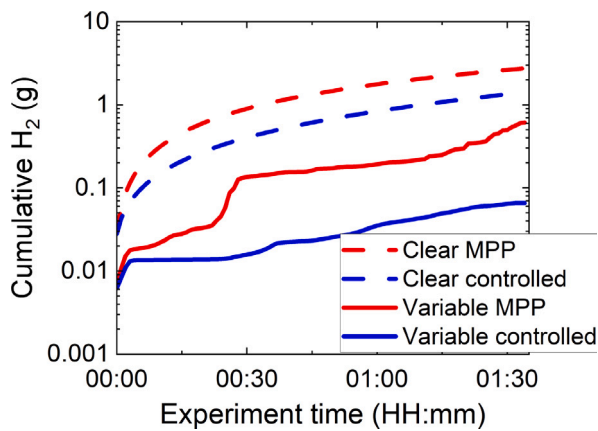


Fig. 10. Theoretical 1-min hydrogen generation of the clear and variable scenarios with and without control. Note that the vertical axis has a logarithmic scale. Although the typical unit used for hydrogen is kg, because hydrogen is very light and its production is low, for clarity's sake, the hydrogen generation is expressed in grams (g).

the same in a very short period is very high, so a simple persistence model could be already an improvement for clear moments. A larger forecasting horizon has the drawback that as the prediction horizon increases, so does the prediction uncertainty. This could result in more ramp violations in exchange for higher energy production because it is possible that the controller misapplies the traditional P&O instead of curtailment in a variable situation.

Fig. 10 shows the effect of our strategy on hydrogen generation. In line with Figs. 7 and 9, the effect of the control strategy on the clear scenario is only a generation reduction, without affecting the generation rate, which remains constant (the hydrogen generation increases linearly with time. Note that the vertical axis is logarithmic). This also occurs with the controlled power of the variable scenario, with the lowest generation. The uncontrolled variable scenario has steep changes. While the electrolyzer can handle these changes in power, other components in the system might have problems with the sudden increase in generation, as they respond slower [6]. Even though this study does not consider the electrolyzer temperature, this variable might determine the hydrogen production efficiency. With steep up ramps, the efficiency might be lower because a higher temperature results in higher efficiency, but the temperature cannot follow the ramps as fast as the changes in the electric set points. Then, the electrolyzer would operate at a higher power with a lower temperature, reducing efficiency.

3.3. Limitations of this study and future improvements

Our study assumes that the irradiance remains constant during each minute, changing only at the top of the minute. In reality, irradiance is not discrete. The measurement system takes images every minute, which justifies the time resolution. Additionally, the hardware emulator is limited to 100 I-V curves per simulation block, making time down-sampling impractical as only a few minutes could be simulated rather than a full hour. The prediction module and the fuzzy logic controllers can still be optimized. The study aims to prove the concept rather than provide a fully optimized system.

Although the prediction module has a low classification accuracy, the system was designed to deal with imperfect predictions, turning the disadvantage of its low accuracy into a tool for analyzing our solution. Naturally, the prediction module can be improved by increasing the number of training points (nearly 28,000 in this study), the number of classification bins and hyperparameter tuning. The dataset consists of many training examples with the sun covered, which might affect the low accuracy of the algorithm. A more balanced dataset can also boost the prediction accuracy.

The approach in this work used empirically determined rules based on the observations of the system. Adding more rules can improve the system's performance, but manual tuning might be cumbersome. Switching to a neuro-fuzzy approach where the shape and position of the membership functions and the inference rules can be determined from training data [30], can facilitate the process and improve the system's performance.

The simulation of the electrolyzer assumes a constant operating temperature, which is only true if there is an external control system. This assumption simplifies the system considerably. In reality, without thermal control, the temperature of the electrolyzer depends on the current flowing through the electrolyzer. At the same time, the current force the applied voltage to change because the current-voltage characteristic of the electrolyzer also depends heavily on temperature.

4. Conclusion

We presented a control strategy for a battery-less stand-alone PV-electrolyzer system to smooth power ramps from the PV system without the need for electrical storage using active power curtailment. This approach typically needs ultra-short-term forecasting to determine the curtailment level. Our control system acknowledges that the prediction is imperfect and incorporates information on the uncertainty to deal with inaccurate predictions using fuzzy logic.

We validated our control strategy with a hardware emulator and prediction from measured data. Using this approach, although it compromises 53% of the potential energy generation, is possible to smooth PV power ramps to a limit of 10% of the PV plant capacity on very high variable moments, and with very imprecise predictions without any storage nor power interruption to the electrolyzer.

CRedit authorship contribution statement

V.A. Martinez Lopez: Writing – original draft, Validation, Software, Methodology, Investigation, Formal analysis, Conceptualization. **O. Isabella:** Writing – review & editing, Resources, Project administration. **M. Zeman:** Resources, Project administration, Funding acquisition. **H. Ziar:** Writing – review & editing, Supervision, Resources.

Declaration of competing interest

The authors declare that they have no known competing financial interests or personal relationships that could have appeared to influence the work reported in this paper.

Data availability

Data will be made available on request.

Acknowledgments

This activity is co-financed by Shell and a PPP-allowance from Top Consortia for Knowledge and Innovation (TKI's) of the Dutch Ministry of Economic Affairs and Climate in the context of the TU Delft e-Refinery program. We kindly thank Stefaan Heirman and dr. Zameer Ahmad for their support with the hardware emulator.

Appendix. Fuzzy rules

- (1) If *uncertainty* is LOW and *predicted ramp* is DEEP DOWN and *previous slope* is POSITIVE BIG then *slope* is NEGATIVE LARGE.
- (2) If *uncertainty* is LOW and *predicted ramp* is DEEP DOWN and ΔGHI is NEGATIVE LARGE and *previous slope* is not NEGATIVE BIG then *slope* is ZERO.
- (3) If *uncertainty* is LOW and *predicted ramp* is DEEP DOWN and ΔGHI is NEGATIVE LARGE and *previous slope* is ZERO then *slope* is ZERO.
- (4) If *uncertainty* is HIGH and ΔGHI is POSITIVE HIGH and *previous slope* is ZERO then *slope* is POSITIVE LARGE.
- (5) If *uncertainty* is HIGH and ΔGHI is NEGATIVE LARGE and *previous slope* is ZERO then *slope* is NEGATIVE LARGE.
- (6) If *uncertainty* is HIGH and ΔGHI is NEGATIVE LARGE and *previous slope* is POSITIVE BIG then *slope* is NEGATIVE LARGE.
- (7) If *uncertainty* is HIGH and ΔGHI is POSITIVE HIGH and *previous slope* is POSITIVE BIG then *slope* is ZERO.
- (8) If *uncertainty* is HIGH and ΔGHI is POSITIVE HIGH and *previous slope* is NEGATIVE BIG then *slope* is POSITIVE LARGE.
- (9) If *uncertainty* is HIGH and ΔGHI is NEGATIVE LARGE and *previous slope* is NEGATIVE BIG then *slope* is POSITIVE LARGE.
- (10) If *uncertainty* is HIGH and ΔGHI is SHALLOW and *previous slope* is NEGATIVE BIG then *slope* is POSITIVE LARGE.
- (11) If *uncertainty* is HIGH and ΔGHI is SHALLOW and *previous slope* is ZERO then *slope* is ZERO.
- (12) If *uncertainty* is HIGH and ΔGHI is SHALLOW and *previous slope* is POSITIVE BIG then *slope* is ZERO.
- (13) If *uncertainty* is LOW and *predicted ramp* is DEEP DOWN and ΔGHI is SHALLOW and *previous slope* is NEGATIVE BIG then *slope* is ZERO.
- (14) If *uncertainty* is LOW and *predicted ramp* is DEEP DOWN and ΔGHI is SHALLOW and *previous slope* is ZERO then *slope* is NEGATIVE LARGE.
- (15) If *uncertainty* is LOW and *predicted ramp* is DEEP DOWN and ΔGHI is POSITIVE HIGH and *previous slope* is NEGATIVE BIG then *slope* is ZERO.
- (16) If *uncertainty* is LOW and *predicted ramp* is DEEP DOWN and ΔGHI is POSITIVE HIGH and *previous slope* is ZERO then *slope* is NEGATIVE LARGE.
- (17) If *uncertainty* is LOW and *predicted ramp* is SHALLOW and ΔGHI is NEGATIVE LARGE then *slope* is ZERO.
- (18) If *uncertainty* is LOW and *predicted ramp* is SHALLOW and ΔGHI is SHALLOW and *previous slope* is NEGATIVE BIG then *slope* is ZERO.
- (19) If *uncertainty* is LOW and *predicted ramp* is SHALLOW and ΔGHI is SHALLOW and *previous slope* is POSITIVE BIG then *slope* is NEGATIVE LARGE.
- (20) If *uncertainty* is LOW and *predicted ramp* is SHALLOW and ΔGHI is SHALLOW and *previous slope* is ZERO then *slope* is ZERO.
- (21) If *uncertainty* is LOW and *predicted ramp* is SHALLOW and ΔGHI is POSITIVE HIGH and *previous slope* is NEGATIVE BIG then *slope* is POSITIVE LARGE.
- (22) If *uncertainty* is LOW and *predicted ramp* is SHALLOW and ΔGHI is POSITIVE HIGH and *previous slope* is ZERO then *slope* is POSITIVE LARGE.
- (23) If *uncertainty* is LOW and *predicted ramp* is SHALLOW and ΔGHI is POSITIVE HIGH and *previous slope* is POSITIVE LARGE then *slope* is ZERO.
- (24) If *uncertainty* is LOW and *predicted ramp* is DEEP UP and ΔGHI is POSITIVE HIGH and *previous slope* is NEGATIVE BIG then *slope* is POSITIVE LARGE.
- (25) If *uncertainty* is LOW and *predicted ramp* is DEEP UP and ΔGHI is POSITIVE HIGH and *previous slope* is ZERO then *slope* is POSITIVE LARGE.

- (26) If *uncertainty* is LOW and *predicted ramp* is DEEP UP and ΔGHI is POSITIVE HIGH and *previous slope* is POSITIVE BIG then *slope* is ZERO.
- (27) If *uncertainty* is LOW and *predicted ramp* is DEEP UP and ΔGHI is NEGATIVE LARGE and *previous slope* is NEGATIVE BIG then *slope* is POSITIVE LARGE.
- (28) If *uncertainty* is LOW and *predicted ramp* is DEEP UP and ΔGHI is NEGATIVE LARGE and *previous slope* is ZERO then *slope* is POSITIVE LARGE.
- (29) If *uncertainty* is LOW and *predicted ramp* is DEEP UP and ΔGHI is NEGATIVE LARGE and *previous slope* is POSITIVE BIG then *slope* is ZERO.
- (30) If *uncertainty* is LOW and *predicted ramp* is DEEP UP and ΔGHI is SHALLOW and *previous slope* is ZERO then *slope* is ZERO.
- (31) If *uncertainty* is LOW and *predicted ramp* is DEEP UP and ΔGHI is SHALLOW and *previous slope* is NEGATIVE BIG then *slope* is POSITIVE LARGE.
- (32) If *uncertainty* is LOW and *predicted ramp* is DEEP DOWN and ΔGHI is SHALLOW and *previous slope* is POSITIVE BIG then *slope* is ZERO.

References

- [1] International Energy Agency, IEA, Renewables 2022, executive summary, 2022, [Online]. Available: <https://www.iea.org/reports/renewables-2022/executive-summary>.
- [2] S. Sukumar, M. Marsadek, K. Agileswari, H. Mokhlis, Ramp-rate control smoothing methods to control output power fluctuations from solar photovoltaic (PV) sources—A review, *J. Energy Storage* 20 (2018) 218–229.
- [3] X. Chen, Y. Du, E. Lim, L. Fang, K. Yan, Towards the applicability of solar nowcasting: A practice on predictive PV power ramp-rate control, *Renew. Energy* 195 (2022) 147–166.
- [4] X. Chen, Y. Du, H. Wen, L. Jiang, W. Xiao, Forecasting-based power ramp-rate control strategies for utility-scale PV systems, *IEEE Trans. Ind. Electron.* 66 (3) (2019) 1862–1871.
- [5] E. Cirés, J. Marcos, I. de la Parra, M. García, L. Marroyo, The potential of forecasting in reducing the LCOE in PV plants under ramp-rate restrictions, *Energy* 188 (2019) 116053.
- [6] V.A. Martinez Lopez, H. Ziar, J. Haverkort, M. Zeman, O. Isabella, Dynamic operation of water electrolyzers: A review for applications in photovoltaic systems integration, *Renew. Sustain. Energy Rev.* 182 (2023) 113407.
- [7] B. Gillesen, H.U. Heinrichs, P. Stenzel, J. Linszen, Hybridization strategies of power-to-gas systems and battery storage using renewable energy, *Int. J. Hydrog. Energy* 42 (19) (2017) 13554–13567.
- [8] A. Gonzalez-Moreno, J. Marcos, I. de la Parra, L. Marroyo, A PV ramp-rate control strategy to extend battery lifespan using forecasting, *Appl. Energy* 323 (2022) 119546.
- [9] H. Wen, Y. Du, X. Chen, E. Lim, H. Wen, L. Jiang, W. Xiang, Deep learning based multistep solar forecasting for PV ramp-rate control using sky images, *IEEE Trans. Ind. Inform.* 17 (2) (2021) 1397–1406.
- [10] Q. Jiang, H. Hong, Wavelet-based capacity configuration and coordinated control of hybrid energy storage system for smoothing out wind power fluctuations, *IEEE Trans. Power Syst.* 28 (2) (2013) 1363–1372.
- [11] M. Saleh, L. Meeq, M.A.S. Masoum, M. Abshar, Battery-less short-term smoothing of photovoltaic generation using sky camera, *IEEE Trans. Ind. Inform.* 14 (2) (2018) 403–414.
- [12] X. Chen, X. Xu, J. Wang, L. Fang, Y. Du, E.G. Lim, J. Ma, Robust proactive power smoothing control of PV systems based on deep reinforcement learning, *IEEE Trans. Sustain. Energy* 14 (3) (2023) 1585–1598.
- [13] Trina Solar, The tallmax 144 framed 144 layout module (datasheet), 2020, [Online]. Available: [https://static.trinasolar.com/sites/default/files/MA_Datasheet_TallmaxM_DE17M\(II\)_202011.pdf](https://static.trinasolar.com/sites/default/files/MA_Datasheet_TallmaxM_DE17M(II)_202011.pdf).
- [14] V.A. Martinez Lopez, H. Ziar, M. Zeman, O. Isabella, Maximization of PV energy use and performance analysis of a stand-alone PV-hydrogen system, *Int. J. Hydrog. Energy* 48 (99) (2023) 39298–39314.
- [15] E.L. Maxwell, A Quasi-Physical Model for Converting Hourly Global Horizontal to Direct Normal Insolation, *Tech. Rep. SERI/TR-215-3087*, Solar Energy Research Institute, Golden, CO, 1987.
- [16] Sandia National Laboratories, PV_LIB Toolbox. [Online]. Available: https://pvpmc.sandia.gov/tools/pv_lib-toolbox/.
- [17] A. Smets, K. Jäger, O. Isabella, R. van Swaaij, M. Zeman, *Solar Energy: The Physics and Engineering of Photovoltaic Conversion, Technologies and Systems*, UIT Cambridge, 2016.
- [18] K. Ishaque, Z. Salam, H. Taheri, Simple, fast and accurate two-diode model for photovoltaic modules, *Sol. Energy Mater. Sol. Cells* 95 (2) (2011) 586–594.

- [19] D.S. Falcão, A.M.F.R. Pinto, A review on PEM electrolyzer modelling: Guidelines for beginners, *J. Clean. Prod.* 261 (2020) 121184.
- [20] Øystein Ulleberg, Modeling of advanced alkaline electrolyzers: a system simulation approach, *Int. J. Hydrog. Energy* 28 (1) (2003) 21–33.
- [21] Chroma, Solar array simulator DC power supply, 2023, [Online]. Available: <https://www.chromausa.com/product/solar-array-simulator/>.
- [22] Imperix, SiC power module PEB8024, 2023, [Online]. Available: <https://imperix.com/products/power/sic-power-module/>.
- [23] Imperix, Passive filters, 2023, [Online]. Available: <https://imperix.com/products/power/filter-box/>.
- [24] Imperix, Rapid prototyping controller B-box RCP, 2023, [Online]. Available: <https://imperix.com/products/control/rapid-prototyping-controller/>.
- [25] A. Cabrera-Tobar, N. Zanatta, M. Aragüés-Peñalba, M. Salles, M. Pozo, O.G. Bellmunt, Active power control of a PV generator for large scale photovoltaic power plant without energy storage, in: 2019 IEEE PES Innovative Smart Grid Technologies Conference - Latin America, ISGT Latin America, 2019, pp. 1–6.
- [26] CMS Shreder, cms ASI-16/51, 2018, [Online]. Available: http://www.schreder-cms.com/en_pdf/ASI-16_InfoBroch.pdf.
- [27] G. Farneböck, Two-frame motion estimation based on polynomial expansion, in: J. Bigun, T. Gustavsson (Eds.), *Image Analysis*, Springer Berlin Heidelberg, Berlin, Heidelberg, 2003, pp. 363–370.
- [28] R. Marquez, C.F. Coimbra, Intra-hour DNI forecasting based on cloud tracking image analysis, *Sol. Energy* 91 (2013) 327–336.
- [29] Tensorflow, Keras applications ResNet50, 2023, [Online]. Available: https://www.tensorflow.org/api_docs/python/tf/keras/applications/resnet50/ResNet50.
- [30] L.H. Tsoukalas, R.E. Uhrig, *Fuzzy and Neural Approaches in Engineering*, John Wiley & Sons, Inc., USA, 1997.
- [31] Y. Chu, M. Li, C.F. Coimbra, Sun-tracking imaging system for intra-hour DNI forecasts, *Renew. Energy* 96 (2016) 792–799.